ACS SENSORS

pubs.acs.org/acssensors Article

Nanoplasmonic Sandwich Immunoassay for Tumor-Derived Exosome Detection and Exosomal PD-L1 Profiling

Chuanyu Wang, Chung-Hui Huang, Zhuangqiang Gao, Jialiang Shen, Jiacheng He, Alana MacLachlan, Chao Ma, Ya Chang, Wen Yang, Yuxin Cai, Yang Lou, Siyuan Dai, Weiqiang Chen, Feng Li,* and Pengyu Chen*

Cite This: https://doi.org/10.1021/acssensors.1c01101 Read Online

ACCESS | Metrics & More | Article Recommendations | Supporting Information

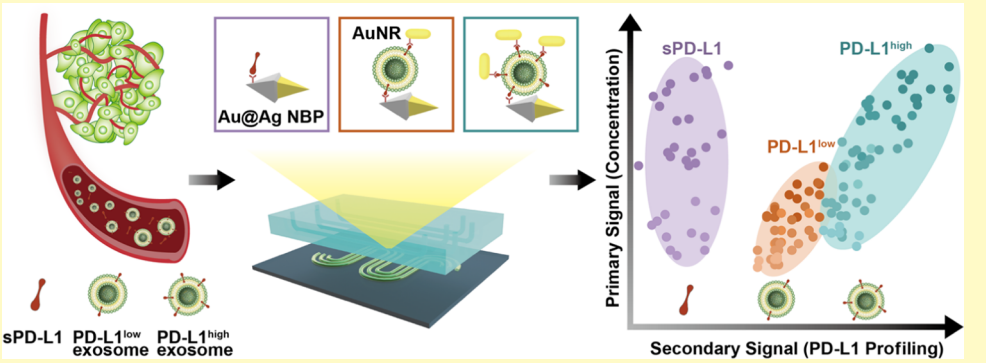

ABSTRACT: Tumor-derived exosomes play a vital role in the process of cancer development. Quantitative analysis of exosomes and exosome-shuttled proteins would be of immense value in understanding cancer progression and generating reliable predictive biomarkers for cancer diagnosis and treatment. Recent studies have indicated the critical role of exosomal programmed death ligand 1 (PD-L1) in immune checkpoint therapy and its application as a patient stratification biomarker in cancer immunotherapy. Here, we present a nanoplasmonic exosome immunoassay utilizing gold−silver (Au@Ag) core−shell nanobipyramids and gold nanorods, which form sandwich immune complexes with target exosomes. The immunoassay generates a distinct plasmonic signal pattern unique to exosomes with specific exosomal PD-L1 expression, allowing rapid, highly sensitive exosome detection and accurate identification of PD-L1 exosome subtypes in a single assay. The developed nanoplasmonic sandwich immunoassay provides a novel and viable approach for tumor cell-derived exosome detection and analysis with quantitative molecular details of key exosomal proteins, manifesting its great potential as a transformative diagnostic tool for early cancer detection, prognosis, and post-treatment monitoring.

KEYWORDS: *exosomes, exosomal protein, programmed death ligand 1 (PD-L1), gold−silver core−shell nanobipyramids (Au@Ag NBPs), localized surface plasmon resonance (LSPR), microfluidics, immunoassay*

Tumor cell-derived exosomes are nanosized extracellular vesicles (EVs) that carry unique surface compositions derived from their cells of origin. These exosomes play essential roles in tumor progression by transferring traits from cancer cells, facilitating intercellular communication, and remodeling a tumor-supportive microenvironment.[1] Exosome-based liquid biopsy has thus become a trending diagnosis option for noninvasive tumor progression monitoring and treatment response evaluation.[2] Recent advancements in large-scale production, purification, and extraction of exosomal contents have revealed multiple important exosome protein biomarkers as promising molecular signatures for cancer diagnosis and treatment.[3] For instance, tumor cells can evade immune surveillance by expressing programmed cell death ligand 1 (PD-L1), which deactivates T cells via interaction with PD-L1 receptors.[4,5] Anti-PD-1 immune checkpoint therapy has thereby shown great potential in treating various types of tumors,[6,7] but the patient response rate remains low.[4,8] Investigations into different forms of extracellular PD-L1, such as those found on the surface expression of tumor-derived exosomes (exosomal PD-L1) or as free soluble PD-L1 proteins (sPD-L1), have suggested that the exosomal PD-L1 exhibits stronger and more robust inhibitory effect on T cells than sPD-

Received: May 27, 2021

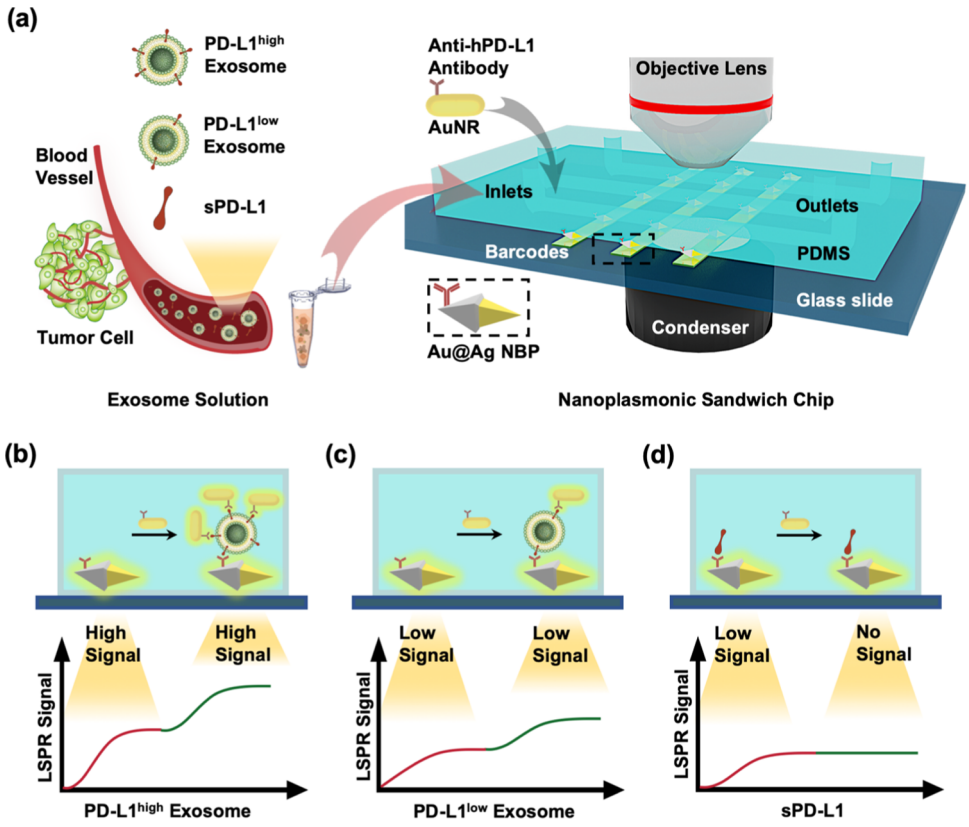

Figure 1. Sensing principle of the nanoplasmonic sandwich immunoassay for exosome quantification and subclass identification. (a) Detection procedure of the nanoplasmonic sandwich immunoassay. Exosome samples containing PD-L1^{high} exosomes, PD-L1^{low} exosomes, or sPD-L1 were first loaded into a microfluidic channel and captured by prepatterned anti-hPD-L1−Au@Ag NBP barcodes for the generation of the primary LSPR signal. Then, anti-hPD-L1−AuNRs were loaded and bound to the exosomal PD-L1 on the captured exosomes for the generation of the secondary LSPR signal. (b−d) Quantification and subclass identification of exosomes based on the generated primary (red curves) and secondary (green curves) LSPR signals. PD-L1^{high} exosomes (b), PD-L1^{low} exosomes (c), and sPD-L1 (d) induce high/high, low/low, and low/no changes for the primary and secondary LSPR signals, respectively.

L1 does. Emerging evidence further indicates that exosomal PD-L1 expression level correlates well with clinical outcomes and could be a valuable predictor for PD-L1 antibody immunotherapy.[3,5,9] Thus, the development of an innovative exosome assay enabling simultaneous exosome detection and exosomal protein profiling could offer in-depth analysis of molecular characteristics of exosomes and advance exosome-based liquid biopsies with improved accuracy for cancer detection and post-treatment prognosis.

Conventional methods, such as enzyme-linked immunosorbent assay (ELISA),[10] Western blot,[11] and flow cytometry,[12] allow quantitative detection of exosomes based on specific surface biomarkers.[13] However, the large sample consumption, insufficient detection sensitivity, and complex instrument requirement have seriously hampered their applications in early tumor diagnosis and tumor prognosis prediction.[14] Considerable effort has been devoted to developing new methods for exosome detection, including colorimetric assays,[15,16] electrochemical detection,[17,18] fluorescence,[19,20] surface plasmon resonance (SPR),[21,22] and integrative microfluidic systems.[23,24] While these approaches have demonstrated remarkable progress in facile, sensitive, and cost-efficient quantification of exosomes, the majority of them still face difficulties in accurate, selective, and quantitative characterization of exosomal proteins. One of the main obstacles for exosomal profiling is the highly heterogeneous nature of exosomes, which are constitutively produced by cells, resulting in varied sizes, molecular compositions, and exosomal expression levels. The interference of the free soluble protein markers, such as sPD-L1, adds another degree of complexity, posing significant challenges for comprehensive exosome analysis and reliable exosome biomarker development in cancer diagnosis and monitoring.

Localized surface plasmon resonance (LSPR)-based nanoplasmonic biosensors have shown great promise in label-free quantitative analysis of exosomes with a limit of detection down to a single exosome.[25] The plasmonic nanoparticles can be readily integrated with dark-field microscopy for subdiffraction imaging, rendering them ideal labeling agents for exosomal proteins with high spatiotemporal resolution.[26] Leveraging the unique advantages of LSPR biosensing and nanoplasmonic labeling, we developed a nanoplasmonic sandwich exosome immunoassay that permits quantitative detection of exosomes and accurate profiling of exosomal proteins (PD-L1) in a single assay. By utilizing the special morphological and compositional characteristics of gold−silver core−shell nanobipyramids (Au@Ag NBPs), we achieved optimum enhancement of LSPR for highly sensitive exosome detection. The addition of antibody-conjugated gold nanorods (AuNRs) bound to the exosomes allows further exosomal protein profiling based on the secondary labeling signals. The nanoplasmonic immunoassay was validated using isolated exosomes from human breast cancer cells and mouse mammary tumor cells with PD-L1 knockout, presenting

https://doi.org/10.1021/acssensors.1c01101
ACS Sens. XXXX, XXX, XXX−XXX

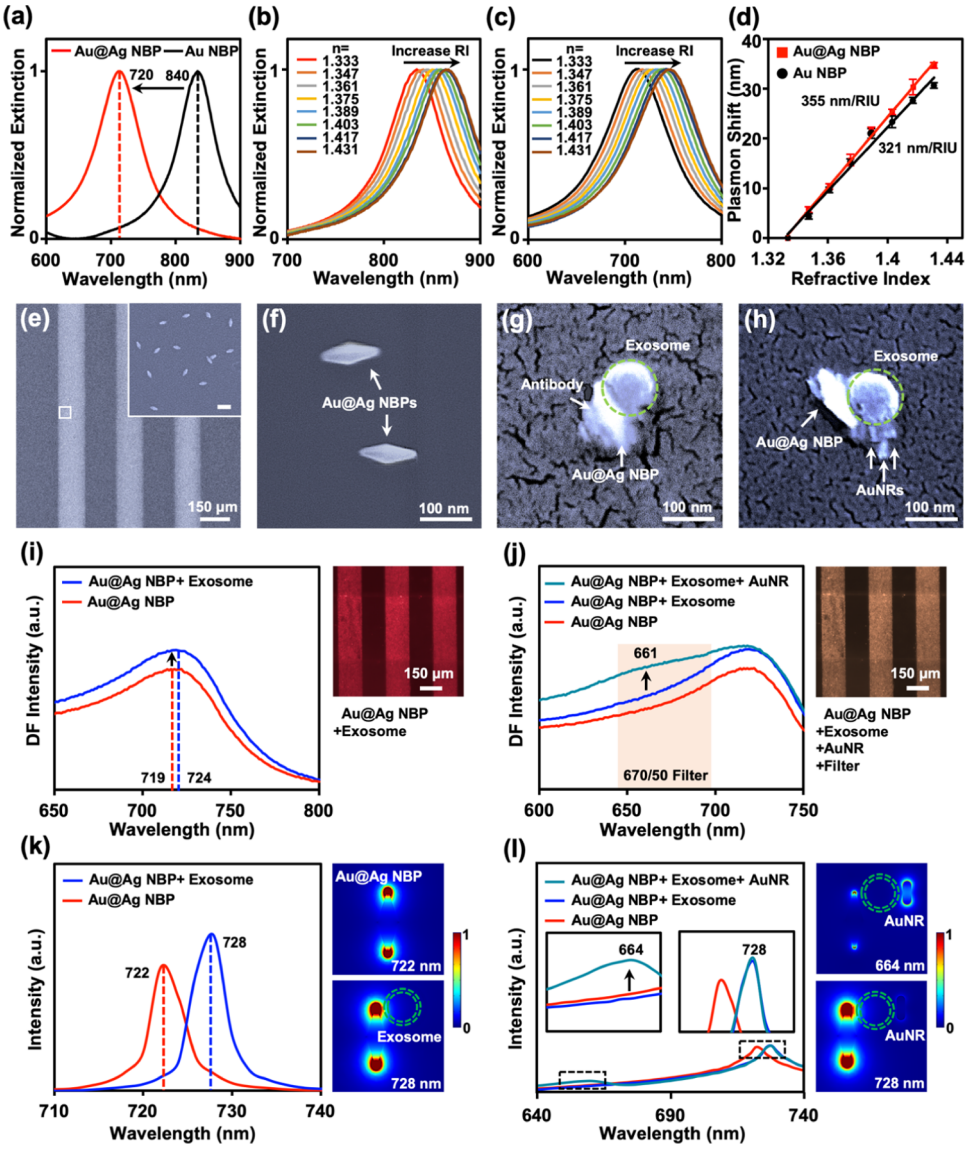

Figure 2. Characterization of the nanoplasmonic sandwich immunoassay. (a) Normalized UV−vis extinction spectra of AuNBPs (black curve) and Au@Ag NBPs (red curve). (b, c) Normalized UV−vis extinction spectra of AuNBPs (b) and Au@Ag NBPs (c) dispersed in water−glycerol mixture solvents with various RIs from 1.333 to 1.431. (d) Linear correlations of AuNBPs (black circles) and Au@Ag NBPs (red squares) generated by plotting the plasmon shift against the RI. (e, f) SEM images of Au@Ag NBP barcodes at low (e) and high (f) magnifications. The inset in panel (e) shows a magnified SEM image of a Au@Ag NBP barcode, scale bar 100 nm. (g, h) SEM images of an anti-hPD-L1−Au@Ag NBP after capturing an exosome (g) and binding with anti-hPD-L1−AuNR conjugates (h). (i, j) Dark-field LSPR scattering spectra of anti-hPD-L1−Au@Ag NBP barcodes before (red curve, i) and after binding with exosomes (blue curve, i) and then with anti-hPD-L1−AuNR conjugates (cyan curve, j). Right panels in (i) and (j) show dark-field images of anti-hPD-L1−Au@Ag NBP barcodes after binding with exosomes (e) and anti-hPD-L1−AuNR conjugates (f). (k, l) COMSOL Multiphysics simulations. Simulated LSPR scattering spectra of a single Au@Ag NBP nanostructure (red curve, k), Au@Ag NBP−exosome nanostructure (blue curve, k), and Au@Ag NBP−exosome−AuNR sandwich nanostructure (cyan curve). Right panels show the corresponding electric field intensity maps of the nanostructures.

distinctive signal patterns characterized by PD-L1 expression levels. The assay was further applied to measure unknown exosome samples to demonstrate it as an accurate, sensitive, and robust approach for the detection and identification of exosome subtypes via exosomal PD-L1 profiling.

RESULTS AND DISCUSSION

Principle of Nanoplasmonic Sandwich Exosome Immunoassay. The sensing principle and procedures of the nanoplasmonic sandwich immunoassay for exosome quantification and subclass identification are summarized in Figure 1. Specifically, the sandwich exosome immunoassay consists of a microfluidic device with three parallel Au@Ag NBP barcodes patterned on a glass substrate. The barcodes are functionalized with anti-human PD-L1 (anti-hPD-L1) antibodies, serving as the primary capture layer in the sandwich structure that binds to the exosomal PD-L1 or sPD-L1 in the loaded sample (Figure 1a). The binding of exosomes/sPD-L1 on the Au@Ag NBPs yields a red-shift of the plasmonic resonance wavelength and a scattering intensity increase due to local refractive index change.[27] The resulting optical responses can be monitored in real-time through an LSPR dark-field imaging technique developed previously by our group for rapid, sensitive exosome/sPD-L1 detection.[28−32] After that, a secondary

https://doi.org/10.1021/acssensors.1c01101
ACS Sens. XXXX, XXX, XXX−XXX

labeling agent, anti-hPD-L1 antibody-functionalized AuNR (anti-hPD-L1−AuNR), will be loaded and bound to the exosomal PD-L1 on the exosomes, forming the sandwich structure. The AuNRs exhibit strong LSPR scattering under dark-field imaging with a distinct resonance wavelength (~660 nm) from that of the Au@Ag NBPs (~720 nm), allowing identification and quantification of exosomal PD-L1 based on the secondary LSPR signal intensity. As a result of the sandwich formation, the whole assay generates a two-step LSPR signal pattern including the following: (1) the exosome binding induces the primary LSPR signal change (red curves in Figure 1b−d) and (2) the labeling of AuNRs on the exosome yields the secondary LSPR signal change (green curves in Figure 1b−d). Since exosomes are relatively large (~100 nm) and display strong optical contrast at the membrane−cytoplasm interface, it is anticipated that the binding of exosomes on the Au@Ag NBPs would result in a much larger initial LSPR signal change (Figure 1b,c) as compared to that from the sPD-L1 binding (Figure 1d). For exosomes with the high expression of exosomal PD-L1 (PD-L1^{high} exosome), abundant exosomal PD-L1 would remain exposed after binding to Au@Ag NBP, leading to a stronger secondary LSPR signal (Figure 1b) than that of exosomes carrying low exosomal PD-L1 (PD-L1^{low} exosome) (Figure 1c). No secondary LSPR signal is expected for sPD-L1 as both the Au@Ag NBPs and the AuNRs are functionalized with the same monoclonal PD-L1 antibodies (Figure 1d). According to this sensing principle, we could clearly differentiate the PD-L1^{high} exosomes, the PD-L1^{low} exosomes, and the sPD-L1 utilizing the distinct LSPR signal patterns generated from the sandwich immunoassay.

Characterization of Nanoplasmonic Sensing Components for the Immunoassay. The sensing performance of the nanoplasmonic sandwich immunoassay is mainly governed by the plasmonic properties of nanoparticles (NPs), including LSPR wavelength, refractive index (RI) sensitivity, and figure of merit (FOM).[33] Previous studies have demonstrated elongated NPs (i.e., gold nanobipyramids (AuNBPs) and AuNRs) as promising nanoplasmonic sensing elements for biomolecular detection with excellent RI sensitivities.[34] Among these, AuNBPs show an ultra-high RI sensitivity (~300 nm/RIU) due to the plasmonic "hot spots" located at the sharp tips,[34] rendering them an ideal candidate for the primary sensing layer in the nanoplasmonic sandwich immunoassay. Here, we coated AuNBPs with Ag layers and synthesized Au@Ag core@shell bipyramidal nanostructures (Au@Ag NBPs) to further improve their RI sensitivity with tunable longitudinal LSPR wavelengths for optimized sensing performance (detailed synthesis procedures can be found in the Materials and Methods section). The formation of Au@Ag NBPs was confirmed by energy-dispersive X-ray spectroscopy (EDS) spectra (Figure S1), high-resolution transmission electron microscopy (HRTEM) images (Figure S2a,b), and a high-angle annular dark-field scanning transmission electron microscopy (STEM-HAADF) image (Figure S2c). The Ag shells (with a slightly brighter contrast in HRTEM images (Figure S2a) and a slightly darker contrast in HAADF-STEM image (Figure S2c)) coated on the AuNBP seeds can be clearly observed owing to the atomic number difference between Ag and Au. The continuous lattice fringes from the Au core to Ag shell (inset in Figure S2b) reveal an epitaxial relationship between the two metals. These results demonstrate the successful formation of Au@Ag core@shell bipyramidal nanostructures.[35,36] A significant blue-shift of the plasmonic wavelength from near-infrared (pristine AuNBPs) to visible range was observed for the Au@Ag NBPs (Figure 2a). Such a blue-shift can be tailored by altering the thickness of the coated silver layer.[37] The electron-multiplying charge-coupled device (EMCCD, Photometrics) used in the LSPR imaging technique for the immunoassay is more sensitive to light in the visible range; therefore, we intentionally selected the Au@Ag NBPs with a Ag shell of ~2 nm for a desired blue resonance shift to ~720 nm. We measured the RI sensitivity of Au@Ag NBPs and AuNBPs by recording the extinction spectrum changes in different water−glycerol mixtures. As the RI increased in the samples, both AuNBPs and Au@Ag NBPs show a red-shift in the longitudinal plasmon wavelengths (Figure 2b,c). The RI sensitivities of the AuNBPs and Au@Ag NBPs were determined to be 321 and 355 nm/RIU, respectively (Figure 2d). The enhanced RI sensitivity after silver coating could be mainly attributed to the lower electromagnetic losses of silver than gold at nanoscale.[38] In addition, the FOM of Au@Ag NBPs was calculated based on the RI sensitivity and the full width at half-maximum (FWHM), showing an extremely high value of 4.4 (the methods for measuring RI sensitivities and FOM of the AuNBPs and Au@Ag NBPs can be found in the Materials and Methods section). These results demonstrate the successful preparation of high-quality Au@Ag NBPs with excellent plasmonic properties.

The as-prepared Au@Ag NBPs were patterned as barcodes on a glass substrate and functionalized with anti-hPD-L1 antibodies for the microfluidic nanoplasmonic chip (Figure S3; detailed Au@Ag NBP barcode patterning procedures can be found in Section 3 in the Supporting Information). Figure 2e shows a representative SEM image of the Au@Ag NBP barcodes. The barcode surface was covered with a monolayer of uniformly distributed Au@Ag NBPs at a particle number density of 19.6 particles/μm^2 (inset in Figure 2e), indicating that the Au@Ag NBPs were monodispersed on the glass surface. These Au@Ag NBPs appear to be very stable on the glass surface as the positively charged Au@Ag NBPs were firmly attached onto the negatively charged glass surface through electrostatic interactions.[28] To verify the functionalization of 11-mercaptoundecanoic acid (MUA) and bioconjugation of anti-hPD-L1 antibodies on Au@Ag NBPs, we utilized Fourier transform infrared (FT-IR) spectroscopy to investigate the Au@Ag NBPs before and after the functionalization and bioconjugation. As shown in Figure S4, no obvious peak was observed for the pristine Au@Ag NBPs from 1000 to 4000 cm^{-1} (red curve). When MUA was functionalized onto the Au@Ag NBPs, the specific peak at 1695 cm^{-1} for MUA was obtained owing to the C═O stretching from carboxylic acids (blue curve), indicating the successful functionalization of MUA on Au@Ag NBPs.[39] When anti-hPD-L1 antibodies were further bioconjugated to the MUA-functionalized Au@Ag NBPs, the characteristic peaks at 1641 and 1557 cm^{-1} special peaks related to amide I region (C═O stretching) and amide II region (N−H bending and C− stretching) of antibodies can be clearly observed (cyan curve), confirming the successful bioconjugation of anti-hPD-L1 antibodies on Au@Ag NBPs.[40] These results confirm the successful biofunctionalization of anti-hPD-L1 antibodies onto Au@Ag NBPs on the barcodes.

AuNRs (~42 nm in length and ~16 nm in diameter; Figure S5a) were conjugated with anti-hPD-L1 antibodies via the EDC/NHS chemistry.[41] The functionalized AuNRs were used as the labeling plasmonic agents to generate the secondary detection signal in the sandwich immunoassay.[41] Since the

https://doi.org/10.1021/acssensors.1c01101
ACS Sens. XXXX, XXX, XXX−XXX

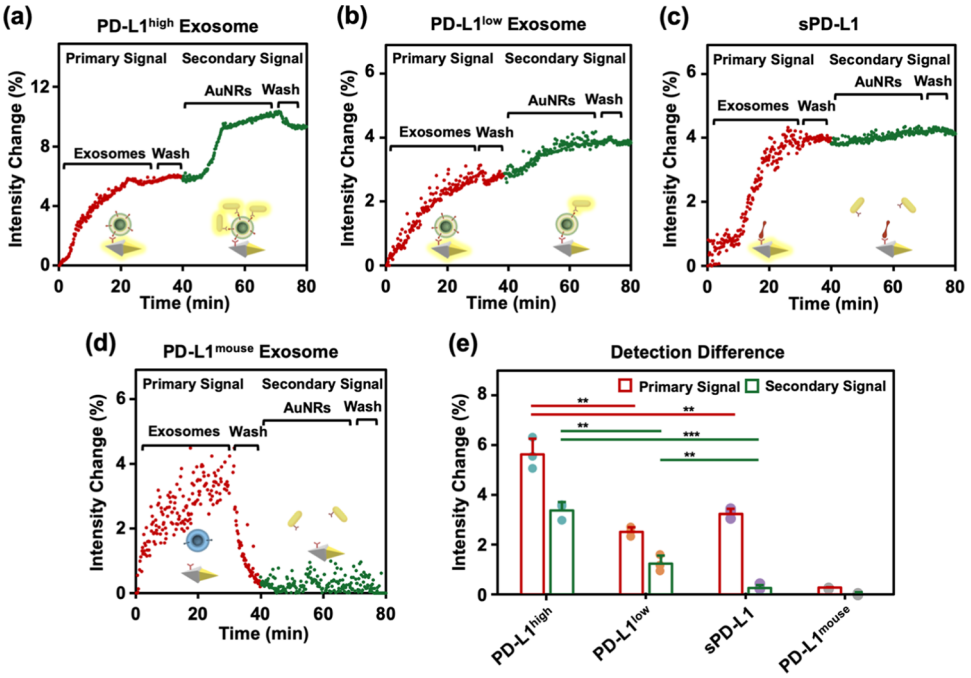

Figure 3. Real-time detection of PD-L1^{high} exosomes, PD-L1^{low} exosomes, sPD-L1, and PD-L1^{mouse} exosomes using the nanoplasmonic sandwich immunoassay. (a–d) Real-time LSPR signal curves showing fractional intensity changes ($\Delta I/I_{0\%}$) for detection of PD-L1^{high} exosomes (a), PD-L1^{low} exosomes (b), sPD-L1 (c), and PD-L1^{mouse} exosomes (d). (e) Corresponding bar graph comparing the fractional intensity changes in the primary signal (red bars) and the secondary signal (green bars) obtained from the measurements. The concentrations of the isolated exosomes and sPD-L1 used in this experiment were 2×10^8 particles/mL and 1 ng/mL, respectively. Statistical analysis of experimental data was performed by a two-sample unpaired *t*-test (*$P < 0.05$, **$P < 0.01$, and ***$P < 0.001$).

average size of the AuNRs was much smaller than those of exosomes (~100 nm) and Au@Ag NBPs (~97 nm in length and ~34 nm in diameter; Figure S5b), multiple anti-hPD-L1–AuNRs can be bound to a single exosome. This results in a concentration-dependent scattering intensity in relation to the level of exosomal PD-L1. Moreover, the anti-hPD-L1–AuNRs exhibit a longitudinal LSPR wavelength at 667 nm, easily distinguishable from that of Au@Ag NBPs (716 nm; Figure S5c). The conjugation of the AuNRs with PD-L1 antibodies was validated by dynamic light scattering (DLS, Malvern Panalytical) and UV–vis spectroscopy. As shown in Figure S5d, the hydrodynamic size of the AuNRs increases significantly from 52.4 to 66.1 nm after functionalization with PD-L1 antibodies, suggesting a single layer of anti-hPD-L1 antibody coating on the surface of AuNRs.[42] The UV–vis spectra of AuNRs and anti-hPD-L1–AuNRs are shown in Figure S5e,f, where a red-shift of the longitudinal wavelength from 663 to 667 nm can be clearly observed for the anti-hPD-L1–AuNR conjugates. The results above demonstrate the successful preparation of the two key plasmonic components (i.e., Au@Ag NBP barcode-based microfluidic chip and anti-hPD-L1–AuNRs) to conduct the nanoplasmonic sandwich immunoassay.

Feasibility of the Nanoplasmonic Sandwich Immunoassay. To validate the feasibility of the nanoplasmonic sandwich immunoassay for exosome detection and exosomal protein profiling, a step-by-step approach using SEM imaging, LSPR scattering spectra, and electromagnetic field simulation (COMSOL Multiphysics) was implemented. The barcode patterns of Au@Ag NBPs on a glass slide as the primary capture layer in the sandwich immunoassay were first validated under SEM (Figure 2e,f). After exosome sample loading, exosomes carrying PD-L1 (green dashed circle) could be captured by anti-hPD-L1 antibody-functionalized Au@Ag NBPs (anti-hPD-L1–Au@Ag NBPs) through the antibody–antigen interaction (Figures 2g and S6a,b). The addition of anti-hPD-L1–AuNR conjugates forming the sandwich-type immunocomplex was also confirmed by SEM (Figures 2h and S6c,d). It should be noted that the stability and monodispersity of Au@Ag NBPs on the glass surface were not significantly affected after incubation with exosomes and then with the anti-hPD-L1–AuNR conjugates. The stepwise binding was further examined by measuring the LSPR scattering spectral change during the sandwich immunoassay. As shown in Figure 2i, the binding of exosomes on Au@Ag NBP barcodes (right panel in Figure 2i) results in a resonance red-shift from 719 to 724 nm and a scattering intensity increase of the longitudinal peak. After loading anti-hPD-L1–AuNR conjugates, a shoulder appears around 661 nm from the spectrum (cyan curve in Figure 2j) of the exosome–Au@Ag NBP barcodes (right panel in Figure 2j), suggesting the formation of the sandwich immunocomplex. As such, the scattering intensity increase due to AuNR binding can be selectively measured using band-pass filters of 670/50 nm as the secondary signals in the sandwich immunoassay. In addition, the electromagnetic field simulations were carried out to provide theoretic understanding of the LSPR spectrum change and guide the design of the sandwich immunoassay (detailed description of the simulation can be found in the Materials and Methods section). The dimensions of the nanostructures used in the simulations were selected in accordance with the previously measured average sizes (Figure S5a,b). For a pristine Au@Ag NBP, enhanced localized electromagnetic (EM) fields were observed at the two sharp tips with a resonance peak centered at 722 nm (upper right in Figure 2k). The attachment of an exosome onto the Au@Ag NBP generates stronger local EM fields with an

https://doi.org/10.1021/acssensors.1c01101
ACS Sens. XXXX, XXX, XXX–XXX

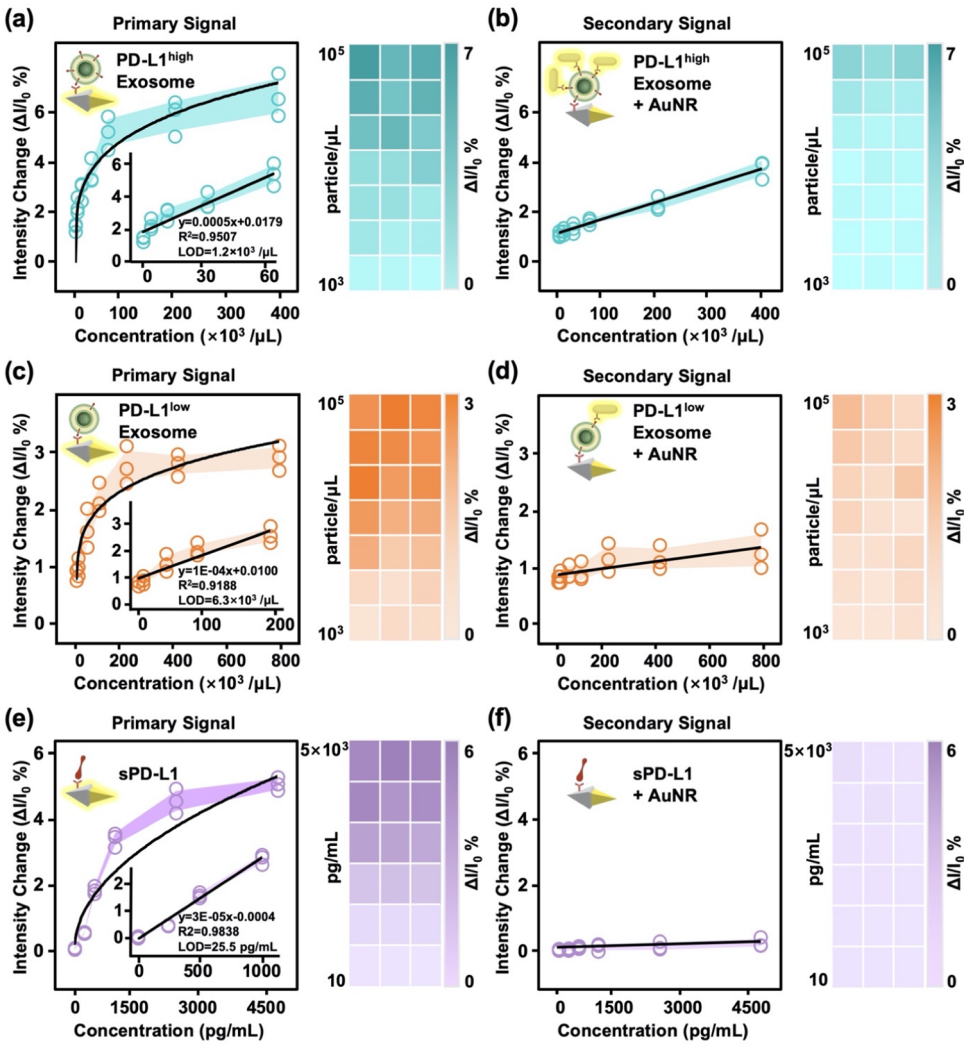

Figure 4. Calibration curves generated by plotting the fractional intensity changes ($\Delta I/I_0$) of the primary signal and secondary signal at different concentrations of PD-L1^{high} exosomes (a, b), PD-L1^{low} exosomes (c, d), and sPD-L1 (e, f). The shaded regions represent $1 - \sigma$ error bands, $n = 3$. The concentration-dependent heat maps were generated based on the primary and secondary signal intensity changes.

increased overall intensity (bottom right in Figure 2k). The calculated LSPR scattering spectra before (red curve in Figure 2k) and after (blue curve in Figure 2k) exosome binding display a spectrum red-shift and thereby a significant scattering intensity increase around 728 nm (the primary signal). The formation of Au@Ag NBP−exosome−AuNR sandwich nanostructure results in the increase of a shoulder-like peak at 664 nm (cyan curve in Figure 2l), which is originated from the longitudinal peak of AuNRs (the secondary signal, right panel in Figure 2l). The slightly broadened shoulder peak in the experimental results could be due to the plasmon coupling of multiple AuNRs binding to the same exosome (Figure 2j). The small discrepancy in the resonance peak positions can be attributed to the variance in NP size and exosome binding location on the NBPs. All of these experiments and simulation results demonstrate the feasibility of the nanoplasmonic sandwich immunoassay for both exosome detection and exosomal PD-L1 profiling based on the selectively filtered primary and secondary signals in a single assay.

Nanoplasmonic Immunoassay for Exosome and Exosomal PD-L1 Detection. The nanoplasmonic sandwich immunoassay was applied to measure three different exosome samples (all at an exosome concentration of 2×10^8 particles/mL) with PD-L1^{high}, PD-L1^{low}, and mouse exosomal PD-L1 knockout (PD-L1^{mouse}) (Figures S7 and S8a,b; detailed exosome isolations and counting procedures can be found in Section 5 in the Supporting Information). A recombinant sPD-L1 sample (1 ng/mL) was also used in the measurement to demonstrate the unique capability of the immunoassay to distinguish exosomal PD-L1 from free sPD-L1 in the solution. For each of the immunoassay measurements, the LSPR signal patterns containing the primary (red curves) and secondary (green curves) signals were recorded in real-time using LSPR imaging and are plotted in Figure 3. When loading PD-L1^{high} exosomes into the barcode-patterned microfluidic chip, the primary signal increased with time owing to the exosome binding on the anti-hPD-L1−Au@Ag NBPs (Figure 3a). The signal reached a plateau after 30 min with a saturated intensity change ($\Delta I/I_0$) of ∼5.9% (detailed intensity change calculations can be found in the Materials and Methods section). No significant decrease was noticed after washing, indicating minimal nonspecific adsorption of exosomes on the sensor surface. Subsequent injection of anti-hPD-L1−AuNRs yielded a secondary signal with a further intensity increase to ∼10.2% after a 30 min incubation (green curve in Figure 3a). The final signal intensity decreased slightly by ∼0.9% due to the removal

https://doi.org/10.1021/acssensors.1c01101
ACS Sens. XXXX, XXX, XXX−XXX

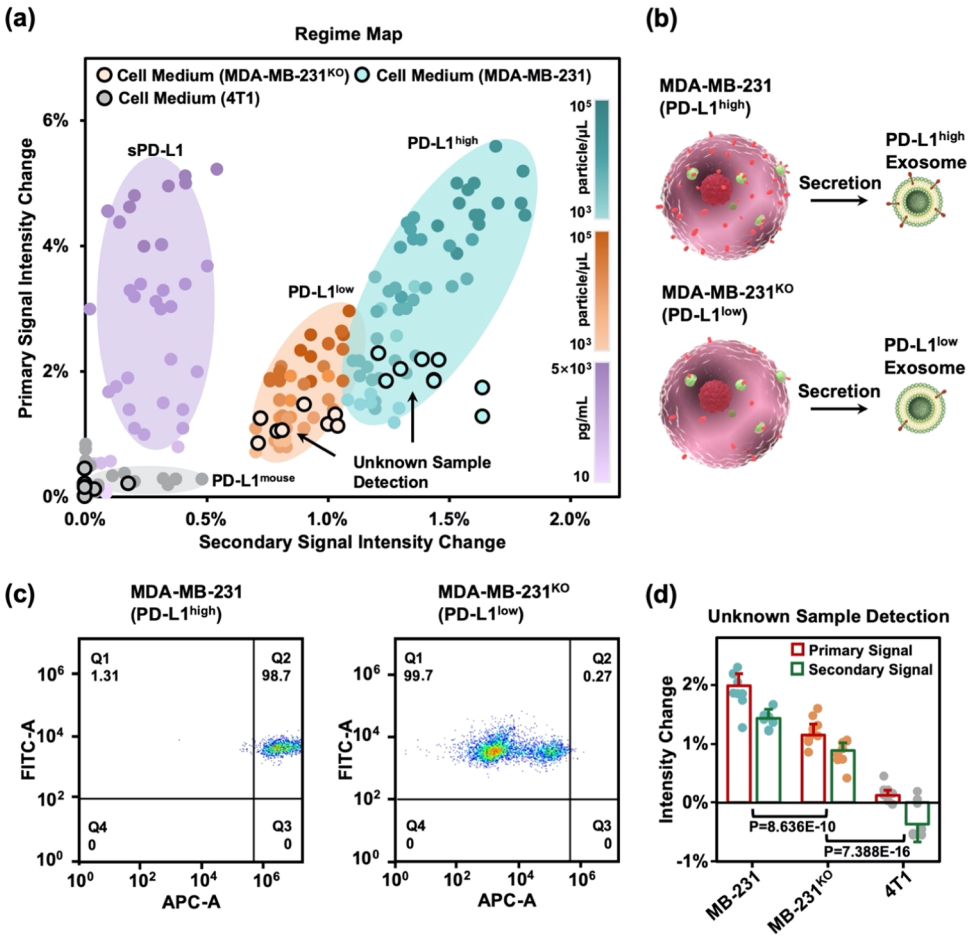

Figure 5. Regime map for exosome subtyping and unknown sample detection. (a) Regime map generated by plotting the primary vs secondary signal intensity changes. The cyan, orange, gray, and purple oval-shaped regions represent subregimes of PD-L1^{high}, PD-L1^{low}, PD-L1^{mouse} exosomes, and sPD-L1, respectively. The color intensities of markers indicate the concentrations of analytes by the color intensity charts. (b) Schematics showing the secretions of PD-L1^{high} and PD-L1^{low} exosomes from MDA-MB-231 and MDA-MB-231^{KO} human cancer cells. (c) Flow cytometry pseudocolor plots showing the PD-L1^{high} on MDA-MB-231 (left) and the PD-L1^{low} on MDA-MB-231^{KO} (right). APC-A and FITC represent the PD-L1 expression and autofluorescence signal from MDA-MB-231, respectively. (d) Bar graph showing the fractional intensity changes in the primary signal (red bars) and the secondary signal (green bars) obtained from detection of unknown cell culture media, n = 3; three experiments were repeated independently. Statistical analysis of experimental data was performed by two-way ANOVA.

of unbound AuNRs after washing. The absolute secondary signal was thus calculated to be 3.4%. The immunoassays were then conducted on PD-L1^{low} exosomes, sPD-L1 samples, and PD-L1^{mouse} exosomes. The primary and absolute secondary signals were measured to be ∼2.8 and ∼1.0%, ∼3.9 and ∼0.2%, and ∼0.2 and ∼0%, respectively (Figure 3b−d). Statistical analysis was further performed to determine the observed difference in the obtained LSPR data from different samples (Figure 3e). As expected, PD-L1^{high} exosomes generated stronger optical responses in both the primary and secondary signals. This could be mainly attributed to the abundant binding sites afforded by the high PD-L1 expression on the exosomes. While for PD-L1^{low} exosomes, the reduced surface expression of PD-L1 resulted in a much lower possibility of exosome binding on the Au@Ag NBP barcodes and the subsequent AuNR labeling. As such, the primary and secondary signal intensities were significantly lower than the signal intensities given by the PD-L1^{high} exosomes. Here, the PD-L1^{mouse} exosomes were used as a negative control, showing negligible final intensity changes in the immunoassay. It should be noted that strong nonspecific adsorption of PD-L1^{mouse} exosomes was observed at the beginning of the immunoassay, which can be readily removed by thorough washing, as evidenced in the real-time LSPR curve (Figure 3d). In addition, the measurement of sPD-L1 proteins displayed an interesting LSPR signal pattern with strong primary binding but no secondary signal. The large primary LSPR intensity increase was mainly induced by the high concentration of sPD-L1 (1 ng/mL) that could fully interact with the monoclonal anti-hPD-L1 antibodies on the Au@Ag NBPs. Unlike the PD-L1 exosomes, no extra binding site of sPD-L1 was available to allow the sandwich structure formation since the secondary labeling AuNRs were conjugated with the same monoclonal antibodies used for the Au@Ag NBPs. Hence, a randomly scattered secondary signal with an absolute value close to 0% was observed.

The nanoplasmonic sandwich immunoassay was further utilized to detect the three different PD-L1 exosome samples and the sPD-L1 solution at varied concentrations (1×10^3−750×10^3 particles/μL for exosomes and 10−5000 pg/mL for sPD-L1). Since the primary and secondary signals are highly dependent on the concentration for exosome binding and AuNR labeling, calibration curves and heat maps for PD-L1^{high}, PD-L1^{low} exosomes, and sPD-L1 were established based on the

https://doi.org/10.1021/acssensors.1c01101
ACS Sens. XXXX, XXX, XXX−XXX

LSPR signal changes at corresponding analyte concentrations (Figure 4). For exosomes carrying PD-L1, the primary signal exhibits a nonlinear increase with an increasing number of exosomes in the sample, showing a Langmuir adsorption characteristic for exosome binding (Figure 4a,c). For the secondary labeling in the immunoassay, an excessive amount of anti-hPD-L1−AuNRs was provided to ensure sandwich complex formation. This resulted in a linear correlation between the secondary signal and the exosome concentration (Figure 4b,d), which can be explained by the reaction-limited binding kinetics. Moreover, the PD-L1 expression level shows a profound effect on the binding of exosomes to the Au@Ag NBP and the subsequent AuNR labeling. The PD-L1^{high} exosomes induced overall stronger LSPR responses in both primary and secondary signals for all of the concentrations in comparison with PD-L1^{low} exosomes (Figure 4a−d). The primary signals for sPD-L1 detection at varied concentrations displayed similar nonlinear behavior to that of the exosome samples (Figure 4e). The secondary signals remain nearly unchanged with increased sPD-L1 concentration due to a lack of AuNR binding (Figure 4f). The linear regions of the calibration curves (insets in Figure 4a,c,e) were plotted, and the primary curves were used to calculate the limits of detection (LODs) of the immunoassay for quantification of PD-L1 exosomes and sPD-L1. Based on the standard $3\sigma/k_{slope}$ method, where σ is the standard derivation of the LSPR signals from blank samples and k_{slope} is the regression slope of the calibration curve, the LODs for PD-L1^{high} and PD-L1^{low} exosomes and sPD-L1 were determined to be 1.2×10^3 particles/μL, 6.3×10^3 particles/μL, and 25.5 pg/mL, respectively. Considering that the average number of exosomes in serum ranged from 10^5 to 10^9/μL,[43,44] our nanoplasmonic sandwich immunoassay achieves an excellent sensitivity that can be potentially used for detection and analysis of exosomes in clinical samples. We have compared the analytical performance (sensitivity, identification target, and sample consumption) of our exosome immunoassay with recently reported exosome detection methods in Table S1. These results indicate that our immunoassay provides a highly sensitive analytical performance for exosome detection as compared to those in the literature and shows minimal sample consumption by taking advantage of the LSPR microfluidic chip. Moreover, it should be emphasized again that our nanoplasmonic sandwich immunoassay could distinguish different types of PD-L1 exosomes through cancer-specific exosomal PD-L1 expression, which has not yet been demonstrated by currently available assays.

Regime Map for Exosome Subtyping and Unknown Sample Detection. Based on the LSPR signal patterns from exosomes and sPD-L1 samples, a regime map was generated by plotting the primary vs the secondary detection signals obtained in the immunoassay. As shown in Figure 5a, there are clearly four defined regions colored in cyan, orange, gray, and purple, corresponding to four different analytes, PD-L1^{high}, PD-L1^{low}, PD-L1^{mouse} exosomes, and sPD-L1, respectively. The color intensity scale in each region represents the associated analyte concentration (intensity scale bars shown in Figure 5a). Specifically, the top-right of the regime map is dominated by PD-L1^{high} exosomes owing to the strong LSPR signals from both primary and secondary detection. The PD-L1^{mouse} exosomes and sPD-L1 occupy the bottom-left corner and the far-left region of the regime map because of limited secondary binding. More importantly, the LSPR signal patterns for PD-L1^{low} exosomes fall in the middle of the regime map, which can be well distinguished from that of PD-L1^{high} exosomes and other samples. As such, the regime map can be used to accurately identify exosome subclasses based on exosomal PD-L1 profiling, as well as distinguish exosomal PD-L1 from free soluble PD-L1 in the sample. As most of the reported sandwich immunoassays utilized a single signal transduction mode to quantify exosomal proteins for exosome characterization,[4,14,45−48] we believe our biosensing principle based on the two-step signal transduction modes could provide a new sensing methodology for characterization of exosomal proteins and thus offer in-depth molecular insights into quantification, identification, and classification of exosome subtypes.

Finally, the nanoplasmonic sandwich immunoassay was validated using exosome samples with unknown PD-L1 expression to demonstrate the use of the regime map for exosome subtyping in real biological samples. Specifically, two types of PD-L1 exosome samples were obtained from the cell culture medium of MDA-MB-231 human breast cancer cells exhibiting high and low PD-L1 expression levels (PD-L1^{high} and PD-L1^{low}), respectively (Figure 5b).[49] Exosomes without any human PD-L1 expression were obtained from the cell culture medium of 4T1 mouse mammary tumor cells with PD-L1 knockout.[49] The PD-L1 expression levels from different cell lines were first confirmed by flow cytometry (Figure 5c). A significant difference was observed in the degree of PD-L1 expression between MDA-MB-231 and MDA-MB-231^{KO}. PD-L1 expression levels from extracted exosomes were determined by Western blot analysis (Figure S8c). PD-L1 level from PD-L1^{high} exosome was significantly higher than that from PD-L1^{low} exosome, while no significant difference was observed in CD63 and GAPDH exosomal markers. The extracted exosome samples from the supernatant of the cell culture medium were measured by the immunoassay. According to the detected primary and secondary signals, the exosome samples were marked as symbols with black borders and placed in their corresponding subregions in the regime map (Figure 5a). Statistical analysis was performed to determine the significant difference between the measured signals from the exosome samples (Figure 5d). The determined PD-L1 exosome subclasses show excellent agreement with the results obtained from flow cytometry, suggesting that tumor cell-derived exosomes share the consistent PD-L1 expression characteristics with their cells of origin. Combining the established calibration curves, the average concentrations of these exosome samples were calculated to be 5.5×10^3 particles/μL (PD-L1^{high} exosome) and 6.5×10^3 particles/μL (PD-L1^{low} exosome), respectively. The analytical recoveries of these samples were measured to be in the range of 78.7−115.6% with coefficients of variation (CVs) of ≤9.38% (n = 3), indicating the high precision of our immunoassay for sensitive exosome quantification (the number of isolated exosomes detected by the nanoparticle tracking analysis (NTA) was used as the reference).

CONCLUSIONS

In conclusion, we have developed a nanoplasmonic sandwich immunoassay that achieves highly sensitive quantification of exosomes and accurate identification of exosome subclasses based on exosomal PD-L1 profiling in real samples. The immunoassay exploits Au@Ag NBPs with a high refractive sensitivity and anti-hPD-L1−AuNRs with strong scattering and distinct plasmonic resonance peak as the two main sensing

https://doi.org/10.1021/acssensors.1c01101
ACS Sens. XXXX, XXX, XXX−XXX

components, yielding high sensitivity and accuracy for exosome detection. The immunoassay was utilized to measure isolated PD-L1 exosomes and spiked sPD-L1. Calibration curves and a subclass regime map were established according to the distinct LSPR signal patterns obtained from the real-time sensing curves. The immunoassay was successfully applied to detect exosome samples derived from cell lines with different levels of PD-L1 expression. The results further demonstrate the unique analytical power of the nanoplasmonic sandwich immunoassay for selective identification, characterization, and determination of exosome subclasses in a single assay using real biological samples. It should be noted that the PD-L1 surface marker can be replaced by any target exosomal protein of interest. As such, the developed nanoplasmonic sandwich immunoassay could be used as a universal platform for tumor cell-derived exosome detection and analysis with great translational potential for a wide range of clinical applications.

MATERIALS AND METHODS

Preparation of Gold Nanobipyramids (AuNBPs). The AuNBPs were prepared using a seed-mediated growth method according to the literature with minor modifications.[34,50] Initially, 0.125 mL of 0.01 M $HAuCl_4$ solution, 0.25 mL of 0.01 M sodium citrate solution, and 9.675 mL of deionized (DI) water were mixed in a 25 mL glass flask and precooled in an ice-water bath under magnetic stirring for 5 min. Then, 0.15 mL of freshly prepared 0.01 M $NaBH_4$ solution was quickly added into the flask, and the mixture was aged at room temperature for 4 h, resulting in the formation of gold nanoseeds. Subsequently, a growth solution was prepared by sequentially adding 0.2 mL of 0.025 M $HAuCl_4$ solution, 0.1 mL of 0.01 M $AgNO_3$ solution, 0.2 mL of 1 M HCl solution, and 0.08 mL of 0.1 M ascorbic acid solution into 10 mL of 0.1 M CTAB solution in a glass vial. After vigorous agitation of the growth solution, 0.1 mL of the above gold nanoseeds was added into the growth solution. The reaction was allowed to proceed at 30 °C in a water bath for 2 h. After being washed with 0.08 M CTAC solution twice via centrifugation, the products (i.e., AuNBPs and Au nanospheres as impurities) were redispersed in 10 mL of 0.08 M CTAC solution. Finally, the AuNBPs were purified from the products using a depletion-induced separation method based on a previously reported procedure[51] and dispersed in 2 mL of 0.05 M CTAB solution.

Synthesis of Au@Ag Core−Shell Nanobipyramids (Au@Ag NBPs). The Au@Ag NBPs were synthesized by overgrowth of Ag on the as-prepared AuNBPs as the seeds, according to the published seed-mediated growth procedures with slight modifications.[37] In a standard synthesis, 0.46 mL of DI water, 0.2 mL of 1 mM $AgNO_3$ solution, 0.52 mL of 0.01 M NaOH solution, and 0.4 mL of 0.01 M ascorbic acid solution were sequentially added into 1 mL of the as-prepared AuNBP suspension. After the reaction at 30 °C for 2 h, the Au@Ag NBPs as products were washed with 0.05 M CTAB solution twice and then redispersed in 1 mL of 0.05 M CTAB solution for future use.

Measurement of Refractive Index (RI) Sensitivities and Figure of Merit (FOM) for AuNBPs and Au@Ag NBPs. Water−glycerol at various volume ratios from 10:0 to 3:7 were mixed with varying RI from 1.333 to 1.431 for the sensitivity measurements. Subsequently, 20 μL of the nanoparticles was dispersed into 980 μL of the water−glycerol mixture. LSPR extinction spectra of the resulting nanoparticle−dispersion solutions were measured using an Ultrospec 2100 pro UV/Visible Spectrophotometer (detailed measurement procedures can be found in Section 2 in the Supporting Information). The plasmon peak shift shown in LSPR extinction spectra was plotted as a function of the RI, and a linear relationship between the plasmon shift and the RI was obtained. The slope of linear regression equation was defined as the RI sensitivity. The RI sensitivities of AuNBPs and Au@Ag NBPs were determined to be 321 and 355 nm/RIU, respectively. The FOM was calculated using the RI sensitivity divided by the full width at half-maximum (FWHM) of the plasmon peak obtained from the aqueous dispersion of nanoparticles. As a result, the FOM of Au@Ag NBPs was calculated to be 355/80 = 4.4.

Fabrication of Au@Ag NBP-Microarray-Based Nanoplasmonic Immunoassay Chip. The procedure for the fabrication of Au@Ag NBP-microarray-based nanoplasmonic immunoassay chip is illustrated in Figure S3. Briefly, a cleaned glass substrate was first treated with oxygen plasma to generate negative charges on its surface. Subsequently, the as-synthesized positively charged Au@Ag NBPs were patterned on the negatively charged glass substrate according to our recently reported microfluidic patterning method[28] via electrostatic interactions between the Au@Ag NBPs and the glass surface. The formed Au@Ag NBP barcode patterns were further functionalized with 11-mercaptoundecanoic acid through Au/Ag−thiol bonding and then modified with anti-hPD-L1 antibodies using the standard EDC/NHS coupling chemistry, resulting in the formation of Au@Ag NBP-microarray-based nanoplasmonic immunoassay chip (detailed fabrication procedures can be found in Section 3 in the Supporting Information).

Preparation of Anti-hPD-L1−AuNR Conjugates. The anti-hPD-L1−AuNR conjugates were prepared by labeling carboxyl-functionalized AuNRs (AuNR-COOH) with anti-hPD-L1 antibodies using the standard EDC/NHS coupling chemistry. In brief, 9 μL of a mixed solution containing 6 μL of 35 mM NHS and 3 μL of 25 mM EDC was added into 100 μL of the AuNR-COOH suspension. After 30 min, the EDC/NHS-activated AuNR-COOH nanoparticles were washed three times with DI water and redispersed in 100 μL of PBS buffer, followed by the addition of 10 μL of 50 μg/mL anti-hPD-L1 antibody solution. After incubation at 4 °C overnight, 20 μL of 10% BSA in PBS buffer was added into the anti-hPD-L1−AuNR reaction suspension. After incubation for 1 h at room temperature, the final products (i.e., anti-hPD-L1−AuNR conjugates) were collected via centrifugation, washed three times with PBS buffer containing 1% BSA and 0.05% Tween 20, redispersed in 2.5 mL of PBS buffer containing 1% BSA and 0.05% Tween 20, and stored at 4 °C for future use.

Nanoplasmonic Sandwich Immunoassay Measurement. An upright dark-field optical microscope (detailed configurations can be found in Section 7 in the Supporting Information) was used for measurements throughout the experiments. In a standard measurement procedure, the as-prepared Au@Ag NBP-microarray-based immunoassay chip was mounted on the motorized stage of the dark-field microscope (Nikon) and an oil immersion dark-field condenser imaging technique was applied. Subsequently, the microfluidic channel was loaded with ∼5 μL of exosome sample at a flow rate of 0.1 μL/min for 30 min, followed by washing with PBS buffer containing 0.05% Tween 20 (PBST) at a flow rate of 1.5 μL/min for 8 min. During this period, the light scattered from the Au@Ag NBP microarrays was collected by the 10× objective lens, imaged by the EMCCD camera, and eventually recorded by NIS-Element BR analysis software. After the washing, ∼5 μL of the anti-hPD-L1−AuNR conjugate solution was injected into the microfluidic channel at a flow rate of 0.1 μL/min for 30 min, filtered by a band-pass filter (ET670/50m, Chroma), and then the channel was washed with PBST at a flow rate of 1.5 μL/min for 8 min, during which the scattered light was recorded again using the same equipment as the first period. Finally, the intensity change ($\Delta I/I_0$) was averaged from the three sensing areas in the microfluidic channel by calculating the signal intensity difference before (I_0) and after ($I_0 + \Delta I$) the sample loading. The sensing areas and calculation were automatically selected and calculated by a customized Matlab program.

Simulations. The theoretical simulations were performed on a single Au@Ag NBP nanostructure, Au@Ag NBP−exosome nanostructure, and Au@Ag NBP−exosome−AuNR sandwich nanostructure using COMSOL Multiphysics. In these simulations, a plane wave with a wavelength of 640−740 nm illuminates the nanostructure with a 2.5−4.5 nm mesh for the calculation of the electric field and extinction spectra. The surrounding medium was set as water with a refractive index of 1.33. The refractive indices of the exosome membrane and interior were 1.48 and 1.38, respectively.[52] And the

https://doi.org/10.1021/acssensors.1c01101
ACS Sens. XXXX, XXX, XXX−XXX

refractive indices of Ag and Au were input from previous works.[53] The nanostructures were modeled according to their morphologies from the TEM data. Specifically, the apexes of the Au@Ag NBP nanostructure were modeled as spherical caps with four cut facets. The diameter and length of the model were 34 and 97 nm, respectively, and the thickness of the Ag was 2 nm. The AuNR was modeled as cylinders with the hemispherical ends where the diameter and length are 16 and 42 nm, respectively. The exosome was modeled as a hollow sphere, with diameter and membrane thickness of 100 and 10 nm, respectively.

■ ASSOCIATED CONTENT

Supporting Information

The Supporting Information is available free of charge at https://pubs.acs.org/doi/10.1021/acssensors.1c01101.

Detailed description, Table S1, and Figures S1−S8 on materials, characterization, RI sensitivity measurement, microarray chip fabrication, cell culture, exosome isolation, Western blot analysis, and FT-IR spectra (PDF)

■ AUTHOR INFORMATION

Corresponding Authors

Feng Li − *Department of Drug Discovery and Development, Harrison School of Pharmacy, Auburn University, Auburn, Alabama 36849, United States;* orcid.org/0000-0002-8559-3831; Phone: 334-844-7406; Email: fzl0023@auburn.edu

Pengyu Chen − *Materials Research and Education Center, Materials Engineering, Department of Mechanical Engineering, Auburn University, Auburn, Alabama 36849, United States;* orcid.org/0000-0003-3380-872X; Phone: 334-844-4913; Email: pengyuc@auburn.edu

Authors

Chuanyu Wang − *Materials Research and Education Center, Materials Engineering, Department of Mechanical Engineering, Auburn University, Auburn, Alabama 36849, United States*

Chung-Hui Huang − *Department of Drug Discovery and Development, Harrison School of Pharmacy, Auburn University, Auburn, Alabama 36849, United States*

Zhuangqiang Gao − *Materials Research and Education Center, Materials Engineering, Department of Mechanical Engineering, Auburn University, Auburn, Alabama 36849, United States;* orcid.org/0000-0001-9097-1799

Jialiang Shen − *Materials Research and Education Center, Materials Engineering, Department of Mechanical Engineering, Auburn University, Auburn, Alabama 36849, United States*

Jiacheng He − *Materials Research and Education Center, Materials Engineering, Department of Mechanical Engineering, Auburn University, Auburn, Alabama 36849, United States*

Alana MacLachlan − *Materials Research and Education Center, Materials Engineering, Department of Mechanical Engineering, Auburn University, Auburn, Alabama 36849, United States*

Chao Ma − *Department of Mechanical and Aerospace Engineering and Department of Biomedical Engineering, New York University, Brooklyn, New York 11201, United States*

Ya Chang − *Department of Drug Discovery and Development, Harrison School of Pharmacy, Auburn University, Auburn, Alabama 36849, United States*

Wen Yang − *Materials Research and Education Center, Materials Engineering, Department of Mechanical Engineering, Auburn University, Auburn, Alabama 36849, United States*

Yuxin Cai − *Materials Research and Education Center, Materials Engineering, Department of Mechanical Engineering, Auburn University, Auburn, Alabama 36849, United States*

Yang Lou − *Yurogen Biosystems LLC, Worcester, Massachusetts 01605, United States*

Siyuan Dai − *Materials Research and Education Center, Materials Engineering, Department of Mechanical Engineering, Auburn University, Auburn, Alabama 36849, United States;* orcid.org/0000-0001-7259-7182

Weiqiang Chen − *Department of Mechanical and Aerospace Engineering and Department of Biomedical Engineering, New York University, Brooklyn, New York 11201, United States;* orcid.org/0000-0002-9469-8328

Complete contact information is available at: https://pubs.acs.org/10.1021/acssensors.1c01101

Author Contributions

P.C. and F.L. conceived the project. C.W. performed the immunoassay fabrication, measurement, and data analysis. C.-H.H. and Y.C. performed the exosome isolation and sample preparation. J.S. and S.D. performed the theoretical simulation. W.Y., J.H., and Y.C. performed the nanomaterial synthesis and characterization. Y.L. provided the PD-L1 antibody and assisted the design of the immunoassay. C.W., A.M., C.M., W.C., S.D., F.L., and P.C. conducted data analysis, writing, reviewing, and editing. All authors provided feedback and agreed on the content of the manuscript.

Notes

The authors declare no competing financial interest.

■ ACKNOWLEDGMENTS

This work was supported by the NIH MIRA R35GM133795 and NSF CAREER CBET-1943302 (P.C.), NIH MIRA R35GM133646 and NSF CBET-1701322 (W.C.), and NSF DMR-2005194 and CPU2AL Seed Grant (J.S., S.D.).

■ REFERENCES

(1) Maia, J.; Caja, S.; Strano Moraes, M. C.; Couto, N.; Costa-Silva, B. Exosome-Based Cell-Cell Communication in the Tumor Microenvironment. *Front. Cell Dev. Biol.* **2018**, *6*, No. 18.

(2) LeBleu, V. S.; Kalluri, R. Exosomes as a Multicomponent Biomarker Platform in Cancer. *Trends Cancer* **2020**, *6*, 767−774.

(3) Daassi, D.; Mahoney, K. M.; Freeman, G. J. The Importance of Exosomal PDL1 in Tumour Immune Evasion. *Nat. Rev. Immunol.* **2020**, *20*, 209−215.

(4) Chen, G.; Huang, A. C.; Zhang, W.; Zhang, G.; Wu, M.; Xu, W.; Yu, Z.; Yang, J.; Wang, B.; Sun, H.; Xia, H.; Man, Q.; Zhong, W.; Antelo, L. F.; Wu, B.; Xiong, X.; Liu, X.; Guan, L.; Li, T.; Liu, S.; Yang, R.; Lu, Y.; Dong, L.; McGettigan, S.; Somasundaram, R.; Radhakrishnan, R.; Mills, G.; Lu, Y.; Kim, J.; Chen, Y. H.; Dong, H.; Zhao, Y.; Karakousis, G. C.; Mitchell, T. C.; Schuchter, L. M.; Herlyn, M.; Wherry, E. J.; Xu, X.; Guo, W. Exosomal PD-L1 Contributes to Immunosuppression and is Associated with anti-PD-1 Response. *Nature* **2018**, *560*, 382−386.

(5) Poggio, M.; Hu, T.; Pai, C. C.; Chu, B.; Belair, C. D.; Chang, A.; Montabana, E.; Lang, U. E.; Fu, Q.; Fong, L.; Blelloch, R. Suppression

of Exosomal PD-L1 Induces Systemic Anti-Tumor Immunity and Memory. *Cell* **2019**, *177*, 414−427.
(6) Sharma, P.; Allison, J. P. The Future of Immune Checkpoint Therapy. *Science* **2015**, *348*, 56−61.
(7) Chen, L.; Han, X. Anti−PD-1/PD-L1 Therapy of Human Cancer: Past, Present, and Future. *J. Clin. Invest.* **2015**, *125*, 3384−3391.
(8) Huang, M.; Yang, J.; Wang, T.; Song, J.; Xia, J.; Wu, L.; Wang, W.; Wu, Q.; Zhu, Z.; Song, Y.; Yang, C. Homogeneous, Low-volume, Efficient, and Sensitive Quantitation of Circulating Exosomal PD-L1 for Cancer Diagnosis and Immunotherapy Response Prediction. *Angew. Chem.* **2020**, *132*, 4830−4835.
(9) Gordon, S. R.; Maute, R. L.; Dulken, B. W.; Hutter, G.; George, B. M.; McCracken, M. N.; Gupta, R.; Tsai, J. M.; Sinha, R.; Corey, D.; Ring, A. M.; Connolly, A. J.; Weissman, I. L. PD-1 Expression by Tumour-Associated Macrophages Inhibits Phagocytosis and Tumour Immunity. *Nature* **2017**, *545*, 495−499.
(10) Logozzi, M.; De Milito, A.; Lugini, L.; Borghi, M.; Calabrò, L.; Spada, M.; Perdicchio, M.; Marino, M. L.; Federici, C.; Iessi, E.; Brambilla, D.; Venturi, G.; Lozupone, F.; Santinami, M.; Huber, V.; Maio, M.; Rivoltini, L.; Fais, S. High Levels of Exosomes Expressing CD63 and Caveolin-1 in Plasma of Melanoma Patients. *PLoS One* **2009**, *4*, No. e5219.
(11) Zhou, H.; Yuen, P. S. T.; Pisitkun, T.; Gonzales, P. A.; Yasuda, H.; Dear, J. W.; Gross, P.; Knepper, M. A.; Star, R. A. Collection, Storage, Preservation, and Normalization of Human Urinary Exosomes for Biomarker Discovery. *Kidney Int.* **2006**, *69*, 1471−1476.
(12) Clayton, A.; Court, J.; Navabi, H.; Adams, M.; Mason, M. D.; Hobot, J. A.; Newman, G. R.; Jasani, B. Analysis of Antigen Presenting Cell Derived Exosomes, Based on Immuno-Magnetic Isolation and Flow Cytometry. *J. Immunol. Methods* **2001**, *247*, 163−174.
(13) Boriachek, K.; Islam, M. N.; Möller, A.; Salomon, C.; Nguyen, N.-T.; Hossain, M. S. A.; Yamauchi, Y.; Shiddiky, M. J. A. Biological Functions and Current Advances in Isolation and Detection Strategies for Exosome Nanovesicles. *Small* **2018**, *14*, No. 1702153.
(14) Zhao, Z.; Yang, Y.; Zeng, Y.; He, M. A Microfluidic ExoSearch Chip for Multiplexed Exosome Detection towards Blood-Based Ovarian Cancer Diagnosis. *Lab Chip* **2016**, *16*, 489−496.
(15) Zhang, Y.; Jiao, J.; Wei, Y.; Wang, D.; Yang, C.; Xu, Z. Plasmonic Colorimetric Biosensor for Sensitive Exosome Detection via Enzyme-Induced Etching of Gold Nanobipyramid@MnO_2 Nanosheet Nanostructures. *Anal. Chem.* **2020**, *92*, 15244−15252.
(16) Boriachek, K.; Masud, M. K.; Palma, C.; Phan, H.-P.; Yamauchi, Y.; Hossain, M. S. A.; Nguyen, N.-T.; Salomon, C.; Shiddiky, M. J. A. Avoiding Pre-Isolation Step in Exosome Analysis: Direct Isolation and Sensitive Detection of Exosomes Using Gold-Loaded Nanoporous Ferric Oxide Nanozymes. *Anal. Chem.* **2019**, *91*, 3827−3834.
(17) Yu, Y.; Li, Y. T.; Jin, D.; Yang, F.; Wu, D.; Xiao, M. M.; Zhang, H.; Zhang, Z. Y.; Zhang, G. J. Electrical and Label-Free Quantification of Exosomes with a Reduced Graphene Oxide Field Effect Transistor Biosensor. *Anal. Chem.* **2019**, *91*, 10679−10686.
(18) Sun, Z.; Wang, L.; Wu, S.; Pan, Y.; Dong, Y.; Zhu, S.; Yang, J.; Yin, Y.; Li, G. An Electrochemical Biosensor Designed by Using Zr-Based Metal−Organic Frameworks for the Detection of Glioblastoma-Derived Exosomes with Practical Application. *Anal. Chem.* **2020**, *92*, 3819−3826.
(19) Wang, X.; Shang, H.; Ma, C.; Chen, L. A Fluorescence Assay for Exosome Detection Based on Bivalent Cholesterol Anchor Triggered Target Conversion and Enzyme-Free Signal Amplification. *Anal. Chem.* **2021**, *93*, 8493−8500.
(20) Li, B.; Pan, W.; Liu, C.; Guo, J.; Shen, J.; Feng, J.; Luo, T.; Situ, B.; Zhang, Y.; An, T.; Xu, C.; Zheng, W.; Zheng, L. Homogenous Magneto-Fluorescent Nanosensor for Tumor-Derived Exosome Isolation and Analysis. *ACS Sens.* **2020**, *5*, 2052−2060.
(21) Liu, C.; Zeng, X.; An, Z.; Yang, Y.; Eisenbaum, M.; Gu, X.; Jornet, J. M.; Dy, G. K.; Reid, M. E.; Gan, Q.; Wu, Y. Sensitive Detection of Exosomal Proteins via a Compact Surface Plasmon Resonance Biosensor for Cancer Diagnosis. *ACS Sens.* **2018**, *3*, 1471−1479.
(22) Fan, Y.; Duan, X.; Zhao, M.; Wei, X.; Wu, J.; Chen, W.; Liu, P.; Cheng, W.; Cheng, Q.; Ding, S. High-Sensitive and Multiplex Biosensing Assay of NSCLC-Derived Exosomes via Different Recognition Sites Based on SPRi Array. *Biosens. Bioelectron.* **2020**, *154*, No. 112066.
(23) Zhang, P.; Zhou, X.; He, M.; Shang, Y.; Tetlow, A. L.; Godwin, A. K.; Zeng, Y. Ultrasensitive Detection of Circulating Exosomes with a 3D-Nanopatterned Microfluidic Chip. *Nat. Biomed. Eng.* **2019**, *3*, 438−451.
(24) Lv, X.; Geng, Z.; Su, Y.; Fan, Z.; Wang, S.; Fang, W.; Chen, H. Label-Free Exosome Detection Based on a Low-Cost Plasmonic Biosensor Array Integrated with Microfluidics. *Langmuir* **2019**, *35*, 9816−9824.
(25) Raghu, D.; Christodoulides, J. A.; Christophersen, M.; Liu, J. L.; Anderson, G. P.; Robitaille, M.; Byers, J. M.; Raphael, M. P. Nanoplasmonic Pillars Engineered for Single Exosome Detection. *PLoS One* **2018**, *13*, No. e0202773.
(26) Wax, A.; Sokolov, K. Molecular Imaging and Darkfield Microspectroscopy of Live Cells Using Gold Plasmonic Nanoparticles. *Laser Photonics Rev.* **2009**, *3*, 146−158.
(27) Anker, J. N.; Hall, W. P.; Lyandres, O.; Shah, N. C.; Zhao, J.; Van Duyne, R. P. Biosensing with Plasmonic Nanosensors. *Nat. Mater.* **2008**, *7*, 442−453.
(28) Chen, P.; Chung, M. T.; McHugh, W.; Nidetz, R.; Li, Y.; Fu, J.; Cornell, T. T.; Shanley, T. P.; Kurabayashi, K. Multiplex Serum Cytokine Immunoassay Using Nanoplasmonic Biosensor Microarrays. *ACS Nano* **2015**, *9*, 4173−4181.
(29) Cai, Y.; Zhu, J.; He, J.; Yang, W.; Ma, C.; Xiong, F.; Li, F.; Chen, W.; Chen, P. Magnet Patterned Superparamagnetic Fe_3O_4 /Au Core−Shell Nanoplasmonic Sensing Array for Label-Free High Throughput Cytokine Immunoassay. *Adv. Healthcare Mater.* **2019**, *8*, No. 1801478.
(30) Javed, I.; He, J.; Kakinen, A.; Faridi, A.; Yang, W.; Davis, T. P.; Ke, P. C.; Chen, P. Probing the Aggregation and Immune Response of Human Islet Amyloid Polypeptides with Ligand-Stabilized Gold Nanoparticles. *ACS Appl. Mater. Interfaces* **2019**, *11*, 10462−10471.
(31) Faridi, A.; Yang, W.; Kelly, H. G.; Wang, C.; Faridi, P.; Purcell, A. W.; Davis, T. P.; Chen, P.; Kent, S. J.; Ke, P. C. Differential Roles of Plasma Protein Corona on Immune Cell Association and Cytokine Secretion of Oligomeric and Fibrillar Beta-Amyloid. *Biomacromolecules* **2019**, *20*, 4208−4217.
(32) Zhu, J.; He, J.; Verano, M.; Brimmo, A. T.; Glia, A.; Qasaimeh, M. A.; Chen, P.; Aleman, J. O.; Chen, W. An Integrated Adipose-Tissue-on-Chip Nanoplasmonic Biosensing Platform for Investigating Obesity-Associated Inflammation. *Lab Chip* **2018**, *18*, 3550−3560.
(33) Potara, M.; Gabudean, A. M.; Astilean, S. Solution-Phase, Dual LSPR-SERS Plasmonic Sensors of High Sensitivity and Stability Based on Chitosan-Coated Anisotropic Silver Nanoparticles. *J. Mater. Chem.* **2011**, *21*, 3625−3633.
(34) Chen, H.; Kou, X.; Yang, Z.; Ni, W.; Wang, J. Shape- and Size-Dependent Refractive Index Sensitivity of Gold Nanoparticles. *Langmuir* **2008**, *24*, 5233−5237.
(35) Yang, Y.; Liu, J.; Fu, Z. W.; Qin, D. Galvanic Replacement-Free Deposition of Au on Ag for Core-Shell Nanocubes with Enhanced Chemical Stability and SERS Activity. *J. Am. Chem. Soc.* **2014**, *136*, 8153−8156.
(36) Gao, Z.; Shao, S.; Gao, W.; Tang, D.; Tang, D.; Zou, S.; Kim, M. J.; Xia, X. Morphology-Invariant Metallic Nanoparticles with Tunable Plasmonic Properties. *ACS Nano* **2021**, *15*, 2428−2438.
(37) Zheng, X.; Chen, Y.; Chen, Y.; Bi, N.; Qi, H.; Qin, M.; Song, D.; Zhang, H.; Tian, Y. High Performance Au/Ag Core/Shell Bipyramids for Determination of Thiram Based on Surface-Enhanced Raman Scattering. *J. Raman Spectrosc.* **2012**, *43*, 1374−1380.
(38) Jakab, A.; Rosman, C.; Khalavka, Y.; Becker, J.; Trügler, A.; Hohenester, U.; Sönnichsen, C. Highly Sensitive Plasmonic Silver Nanorods. *ACS Nano* **2011**, *5*, 6880−6885.

https://doi.org/10.1021/acssensors.1c01101
ACS Sens. XXXX, XXX, XXX−XXX

(39) Amoli, B. M.; Gumfekar, S.; Hu, A.; Zhou, Y. N.; Zhao, B. Thiocarboxylate Functionalization of Silver Nanoparticles: Effect of Chain Length on the Electrical Conductivity of Nanoparticles and Their Polymer Composites. *J. Mater. Chem.* **2012**, *22*, 20048−20056.
(40) Ríos-Corripio, M. A.; Arcila-Lozano, L. S.; Garcia-Perez, B. E.; Jaramillo-Flores, M. E.; Hernández-Pérez, A. D.; Carlos-Martínez, A.; Rosales-Perez, M.; Rojas-López, M. Fluorescent Gold Nanoparticle-Based Bioconjugate for the Detection of Salmonella. *Anal. Lett.* **2016**, *49*, 1862−1873.
(41) Qian, X.; Peng, X. H.; Ansari, D. O.; Yin-Goen, Q.; Chen, G. Z.; Shin, D. M.; Yang, L.; Young, A. N.; Wang, M. D.; Nie, S. In Vivo Tumor Targeting and Spectroscopic Detection with Surface-Enhanced Raman Nanoparticle Tags. *Nat. Biotechnol.* **2008**, *26*, 83−90.
(42) Liu, X.; Dai, Q.; Austin, L.; Coutts, J.; Knowles, G.; Zou, J.; Chen, H.; Huo, Q. A One-Step Homogeneous Immunoassay for Cancer Biomarker Detection Using Gold Nanoparticle Probes Coupled with Dynamic Light Scattering. *J. Am. Chem. Soc.* **2008**, *130*, 2780−2782.
(43) Sina, A. A. I.; Vaidyanathan, R.; Dey, S.; Carrascosa, L. G.; Shiddiky, M. J. A.; Trau, M. Real Time and Label Free Profiling of Clinically Relevant Exosomes. *Sci. Rep.* **2016**, *6*, No. 30460.
(44) Liu, C.; Zhao, J.; Tian, F.; Cai, L.; Zhang, W.; Feng, Q.; Chang, J.; Wan, F.; Yang, Y.; Dai, B.; Cong, Y.; Ding, B.; Sun, J.; Tan, W. Low-Cost Thermophoretic Profiling of Extracellular-Vesicle Surface Proteins for the Early Detection and Classification of Cancers. *Nat. Biomed. Eng.* **2019**, *3*, 183−193.
(45) He, F.; Wang, J.; Yin, B.-C.; Ye, B.-C. Quantification of Exosome Based on a Copper-Mediated Signal Amplification Strategy. *Anal. Chem.* **2018**, *90*, 8072−8079.
(46) Jeong, S.; Park, J.; Pathania, D.; Castro, C. M.; Weissleder, R.; Lee, H. Integrated Magneto-Electrochemical Sensor for Exosome Analysis. *ACS Nano* **2016**, *10*, 1802−1809.
(47) Im, H.; Shao, H.; Park, Y. Il.; Peterson, V. M.; Castro, C. M.; Weissleder, R.; Lee, H. Label-Free Detection and Molecular Profiling of Exosomes with a Nano-Plasmonic Sensor. *Nat. Biotechnol.* **2014**, *32*, 490−495.
(48) Doldán, X.; Fagúndez, P.; Cayota, A.; Laíz, J.; Tosar, J. P. Electrochemical Sandwich Immunosensor for Determination of Exosomes Based on Surface Marker-Mediated Signal Amplification. *Anal. Chem.* **2016**, *88*, 10466−10473.
(49) Yang, Y.; Li, C. W.; Chan, L. C.; Wei, Y.; Hsu, J. M.; Xia, W.; Cha, J. H.; Hou, J.; Hsu, J. L.; Sun, L.; Hung, M. C. Exosomal PD-L1 Harbors Active Defense Function to Suppress T Cell Killing of Breast Cancer Cells and Promote Tumor Growth. *Cell Res.* **2018**, *28*, 862−864.
(50) Lee, K. S.; El-Sayed, M. A. Gold and Silver Nanoparticles in Sensing and Imaging: Sensitivity of Plasmon Response to Size, Shape, and Metal Composition. *J. Phys. Chem. B* **2006**, *110*, 19220−19225.
(51) Li, Q.; Zhuo, X.; Li, S.; Ruan, Q.; Xu, Q. H.; Wang, J. Production of Monodisperse Gold Nanobipyramids with Number Percentages Approaching 100% and Evaluation of Their Plasmonic Properties. *Adv. Opt. Mater.* **2015**, *3*, 801−812.
(52) Van Der Pol, E.; Van Gemert, M. J. C.; Sturk, A.; Nieuwland, R.; Van Leeuwen, T. G. Single vs. Swarm Detection of Microparticles and Exosomes by Flow Cytometry. *J. Thromb. Haemostasis* **2012**, *10*, 919−930.
(53) Johnson, P. B.; Christy, R. W. Optical Constant of the Nobel Metals. *Phys. Rev. B* **1972**, *6*, 4370−4379.

https://doi.org/10.1021/acssensors.1c01101
ACS Sens. XXXX, XXX, XXX−XXX